

PCCP

Accepted Manuscript



This is an *Accepted Manuscript*, which has been through the Royal Society of Chemistry peer review process and has been accepted for publication.

Accepted Manuscripts are published online shortly after acceptance, before technical editing, formatting and proof reading. Using this free service, authors can make their results available to the community, in citable form, before we publish the edited article. We will replace this *Accepted Manuscript* with the edited and formatted *Advance Article* as soon as it is available.

You can find more information about *Accepted Manuscripts* in the [Information for Authors](#).

Please note that technical editing may introduce minor changes to the text and/or graphics, which may alter content. The journal's standard [Terms & Conditions](#) and the [Ethical guidelines](#) still apply. In no event shall the Royal Society of Chemistry be held responsible for any errors or omissions in this *Accepted Manuscript* or any consequences arising from the use of any information it contains.

Palladium local structure of $\text{La}_{1-x}\text{Sr}_x\text{Co}_{1-y}\text{Fe}_{y-0.03}\text{Pd}_{0.03}\text{O}_{3-\delta}$ perovskites synthesized by one pot citrate method

Fabrizio Puleo^a, Leonarda F. Liotta^{b*}, Valeria La Parola^b, Dipanjan Banerjee^c, Antonino Martorana^{a,b} and Alessandro Longo^{b,d*}

Received (in XXX, XXX) Xth XXXXXXXXXX 200X, Accepted Xth XXXXXXXXXX 200X

First published on the web Xth XXXXXXXXXX 200X

DOI: 10.1039/b000000000x

Nanostructured $\text{La}_{1-x}\text{Sr}_x\text{Co}_{1-y}\text{Fe}_{y-0.03}\text{Pd}_{0.03}\text{O}_{3-\delta}$ (LSCF-Pd) perovskites with fixed La-Sr composition ($x=0.4$) and two different Fe contents ($y=0.2$ and 0.8) were successfully prepared by one pot synthesis with citrate method starting from nitrates of the metal cations. Pd-free $\text{La}_{1-x}\text{Sr}_x\text{Co}_{1-y}\text{Fe}_y\text{O}_{3-\delta}$ (LSCF) systems were prepared for comparison. LSCF powders were calcined at $1300\text{ }^\circ\text{C}$ and characterized by XRD and Rietveld refinement, EXAFS, XPS, TPR analyses. Promotion of $\text{La}_{0.6}\text{Sr}_{0.4}\text{Co}_{0.8}\text{Fe}_{0.2}\text{O}_{3-\delta}$ and of $\text{La}_{0.6}\text{Sr}_{0.4}\text{Co}_{0.2}\text{Fe}_{0.8}\text{O}_{3-\delta}$ by incorporation of palladium was evidenced by solving the local environment of Pd using EXAFS spectroscopy. XPS analyses, in agreement with TPR measurements, demonstrated an increase of superficial oxygen vacancies, the variation being much more pronounced in the $\text{La}_{0.6}\text{Sr}_{0.4}\text{Co}_{0.8}\text{Fe}_{0.17}\text{Pd}_{0.03}\text{O}_{3-\delta}$ sample. It is argued that this increase is associated to the introduction of Pd in the B site of LSCF. Moreover, ionic Pd^{4+} was detected as the only palladium species on the perovskite surface, whereas Pd metal clusters of about 2 nm, not detectable in the surface, are embedded in the matrix and strongly interacting with the bulk. This result has strong consequences in the synthesis and in the design of new perovskite materials that can be used as cathode in fuel cell application at intermediate operating temperatures.

Introduction

Solid oxide fuel cells, SOFCs, based on oxide-ion conducting electrolyte, have several advantages over conventional energy systems giving high efficiency in electrical energy and heat production with negligible emissions. However, high standard operating temperature, around $1000\text{ }^\circ\text{C}$, involves high costs and materials degradation that could be overcome at the intermediate temperature (IT) regime of $500\text{--}700\text{ }^\circ\text{C}$. At the sought-after intermediate working temperatures, the catalytic performance and ionic conductivity of both SOFC electrodes must be strongly improved, while the exploitation of renewable hydrocarbon fuels requires the development of electrode materials with improved tolerance to sulphur and carbon poisoning¹⁻⁶. In particular, the current limitation in the final performance of IT-SOFCs is related to the electrochemical processes taking place at the cathode that constitute the bottleneck of an efficient SOFC device.

In recent years, great efforts have been devoted to improve the cathode kinetics by developing new IT-SOFC electrocatalysts. Due to their high mixed ionic and electronic conductivity, perovskite oxides based on lanthanum strontium cobalt ferrite (LSCF) are the most studied mixed ionic and electronic conducting (MIEC) materials for cathode applications in solid oxide fuel cells operated in the intermediate temperature range.^{1,4} The properties of LSCF materials depend very much on their composition: the presence of Sr increases electronic and ionic conductivity, while Fe narrows the thermal expansion coefficient (TEC), but also lowers conductivity. Therefore an optimal composition

for LSCF cathode should arise from a compromise between high electronic and ionic conductivity and suitably low TEC. Recently, it has been reported that the performance of a LSCF cathode can be further enhanced by addition of a small amount of nano-sized noble metals such as Ag or Pd.⁶⁻⁹ The overall cell resistance can be decreased by 15.5% at $650\text{ }^\circ\text{C}$ and by 40% at $550\text{ }^\circ\text{C}$ by impregnating Pd into the LSCF cathode. Adding small amounts of precious metals into a LSCF cathode is also shown to reduce its electrode polarization resistance.¹

The beneficial effect of Pd addition was already observed in the ferrites-based materials developed for self-regenerative automotive emission catalysts which were investigated for NO reduction by C_3H_6 .^{9,10} In a seminal X-ray absorption and X-ray anomalous diffraction study, this effect was attributed to the incorporation of trivalent or tetravalent Pd in the B-site of the perovskite structure.¹¹

The structural results obtained for $\text{LaFe}_{0.57}\text{Co}_{0.38}\text{Pd}_{0.05}\text{O}_{3-\delta}$ ¹¹ were supposed to hold also for Pd/LSCF to explain the enhanced reversibility of these SOFC cathode materials during the reduction cycles involving oxygen species.¹ However, so far a detailed investigation of the chemical environment of Pd in Pd/LSCF systems is lacking. The present study reports the preparation of $\text{La}_{1-x}\text{Sr}_x\text{Co}_{1-y}\text{Fe}_{y-0.03}\text{Pd}_{0.03}\text{O}_{3-\delta}$ oxides by one pot sol-gel citrate method. The La-Sr composition was kept fixed ($x=0.4$), while two different Fe contents ($y=0.2$ and 0.8 respectively) and constant Pd amount of 0.03 were adopted. Pd-free reference samples, $\text{La}_{1-x}\text{Sr}_x\text{Co}_{1-y}\text{Fe}_y\text{O}_{3-\delta}$, were also synthesized with the same one-pot procedure. X-ray diffraction was used to check the syntheses

for the presence of secondary crystalline phases. Complementary data coming from X-ray absorption and X-ray photoelectron spectroscopy allowed a thorough analysis of Pd oxidation state and oxygen defectivity in Pd/LSCF materials. Moreover, comparison with Pd-free compounds in TPR cycles shed light over the role of Pd in the enhancement of the electrocatalytic properties of LSCF. OSC and TGA experiments evidenced the role of Pd in increasing the oxygen vacancy content of LSCF perovskites. These results can have interesting consequences in the design and synthesis of new perovskite cathode materials for fuel cell application at intermediate operating temperatures.

Experimental

Preparation of LSCF materials

All $\text{La}_{1-x}\text{Sr}_x\text{Co}_{1-y}\text{Fe}_y\text{O}_{3-\delta}$ perovskites were synthesized by sol-gel citrate method starting from $\text{La}(\text{NO}_3)_3 \cdot 6\text{H}_2\text{O}$, $\text{Sr}(\text{NO}_3)_2$, $\text{Co}(\text{NO}_3)_2 \cdot 6\text{H}_2\text{O}$, $\text{Fe}(\text{NO}_3)_3 \cdot 9\text{H}_2\text{O}$ as precursors.¹² The metal nitrates, weighed in order to obtain the nominal compositions of $\text{La}_{0.6}\text{Sr}_{0.4}\text{Co}_{0.8}\text{Fe}_{0.2}\text{O}_{3-\delta}$ (labeled as LSCF0.2) and $\text{La}_{0.6}\text{Sr}_{0.4}\text{Co}_{0.2}\text{Fe}_{0.8}\text{O}_{3-\delta}$ (LSCF0.8), were dissolved in a minimum quantity of deionized water. Citric acid (molar ratio of citric acid/metals = 1.5) was added to this solution and finally ammonia (28 - 30%) was dripped until pH 9 - 10. The resulting solution was dehydrated in oil bath at 90 °C to form a sol, followed by a further heating at 120 °C to yield a gel. The so obtained gel was calcined at 350 °C for 1 h, to favour citrate decomposition, and then at 800 °C for 4 h to promote a preliminary crystallization; finally, the temperature was raised to 1300 °C at a rate of 5 °C/min and the samples were kept at this temperature for 4h. $\text{La}_{0.6}\text{Sr}_{0.4}\text{Co}_{0.8}\text{Fe}_{0.17}\text{Pd}_{0.03}\text{O}_{3-\delta}$ (LSCF0.2-Pd) and $\text{La}_{0.6}\text{Sr}_{0.4}\text{Co}_{0.2}\text{Fe}_{0.77}\text{Pd}_{0.03}\text{O}_{3-\delta}$ (LSCF0.8-Pd) were also prepared and calcined, in the same conditions as above described, using $\text{Pd}(\text{NO}_3)_2 \cdot x\text{H}_2\text{O}$ as palladium precursor along with the other metal nitrates. The amount of Pd (3 mol%) in the perovskites corresponds to 1.45 wt%. Elemental analysis of the perovskite oxides was performed by inductively coupled plasma optical emission spectroscopy (ICP-OES), using an ICP Perkin-Elmer Optima 3000DV spectrometer. The powders were dissolved in concentrated HNO_3 at 60 °C and then evaporated almost until dryness. Diluted water solutions of the extracted metal nitrates were analyzed quantitatively by comparison with standard solutions. The real composition corresponded well to the nominal content within $\pm 5\%$.

X-ray Diffraction

XRD measurements were carried out with a Bruker D5000 vertical goniometer equipped with Cu anode ($K\alpha$ radiation = 1.5418 Å) and a graphite monochromator. A proportional counter and a 0.03° step size in 2θ were used. The integration time was 40 seconds per step and the scan range was from 20 to 120° in 2θ . Rietveld refinement on the XRD data were analyzed according to the GSAS program.¹³

Extended X-ray Absorption Fine Structure (EXAFS)

Pd K-edge EXAFS and XANES spectra of LSCF0.2-Pd and

LSCF0.8-Pd were collected at the Dutch-Belgian Beam Line (DUBBLE) at the European Synchrotron Radiation Facility (ESRF).¹⁴ The spectra of the samples (pellets diluted to suitable concentration with Boron Nitride to avoid self absorption) were collected in fluorescence mode using a 9-element Ge detector (Ortec Inc.), whereas reference spectra of the metal Pd foil were collected in transmission mode using Ar/He-filled ionization chambers at ambient temperature and pressure. The energy of the X-ray beam was tuned by a double-crystal monochromator operating in fixed-exit mode using a Si(111) crystal pair. The samples were measured in a closed-cycle He-cryostat (Oxford Instruments) at 80 K to minimize the noise induced by thermal Debye-Waller factor. The EXAFS spectra, three scans per sample, were energy-calibrated, averaged and then analyzed using GNXAS.^{15,16} In this approach, the local atomic arrangement around the absorbing atom is decomposed into model atomic configurations containing 2, ..., n atoms. The theoretical EXAFS signal $\chi(k)$ is given by the sum of the n -body contributions $\gamma^2, \gamma^3, \dots, \gamma^n$, which take into account all the possible single and multiple scattering (MS) paths between the n -atom configurations. The fitting of $\chi(k)$ to the experimental EXAFS signal allows to refine the relevant structural parameters of the different coordination shells; the suitability of the model is also evaluated by comparison of the experimental EXAFS signal Fourier transform (FT) with the FT of the calculated $\chi(k)$ function. The allowed model parameters were coordination numbers, coordination distances, Debye-Waller factors and angles of the γ^n contributions which were defined according to the crystallographic structures used in the data analysis. The Pd K-edge threshold energy was kept fixed at 24350 eV.

X-ray photoelectron spectroscopy (XPS)

The XPS analyses were performed with a VG Microtech ESCA 3000 Multilab, equipped with a dual Mg/Al anode. The spectra were collected using a non-monochromatized Al $K\alpha$ source (1486.6 eV). The analyzer was operated in constant analyzer energy (CAE) mode. For the individual peak energy regions, a pass energy of 20 eV was used. Survey spectra were measured at 50 eV pass energy. The sample powders were mounted on a double-sided adhesive tape. The pressure in the analysis chamber was in the range of 10^{-8} Torr during data collection. All peak energies were calibrated to the C 1s binding energy of adventitious carbon at 285.1 eV. The invariance of the peak shapes and widths at the beginning and at the end of the analyses ensured absence of differential charging. Peak fitting procedures were performed with the software provided by VG, based on non-linear least squares fitting program using a weighted sum of Lorentzian and Gaussian component curves after background subtraction according to Shirley and Sherwood.^{17,18} Atomic concentrations were calculated from peak intensity using the sensitivity factors provided with the software. The binding energy values are reported with a precision of ± 0.15 eV and the atomic percentages with a precision of $\pm 10\%$.

Temperature programmed reduction (TPR)

Temperature programmed reduction (TPR) experiments were carried out with a Micromeritics Autochem 2910 apparatus equipped with a thermal conductivity detector (TCD). The gas mixture with composition 5% H₂ in Ar (50 mL/min) was used to reduce the samples (30 mg), heating from room temperature to 1200 °C at the rate of 10 °C / min. Before starting the TPR analyses, the catalysts were pretreated with a flowing gas mixture of 5% O₂ in He (50 mL/min) at 550 °C for 30 min, and subsequent cooling down under Ar.

Oxygen storage capacity (OSC) and Thermogravimetric analysis (TGA)

The oxygen storage capacity (OSC) measurements were carried out with a Micromeritics Autochem 2910 apparatus on the samples (200 mg) pretreated under He (50 ml/min) at 750 °C for 1h, after cooling down at 600 °C. At this stable temperature pulses of O₂ 5%/He (loop of 1 ml) were injected at regular intervals over the samples flowed under He (30 ml/min), until the break-through point was attained, as detected by TCD analysis.

Thermogravimetric analyses (TGA) were performed with a TGA/DSC1 STAR[®] system METTLER TOLEDO. The samples (10 mg) were pretreated under N₂ (30 ml/min) at 750 °C for 1h; after cooling down to room temperature in air (30 ml/min), the samples were purged for 30 min under N₂ (30ml/min) and then the TGA experiments were carried out under N₂ (30ml/min) by heating (5°C/min) from room temperature up to 1100 °C. The evolution gas species was monitored by on line mass quadrupole(ThermostatTM, Balzers).

RESULTS

XRD

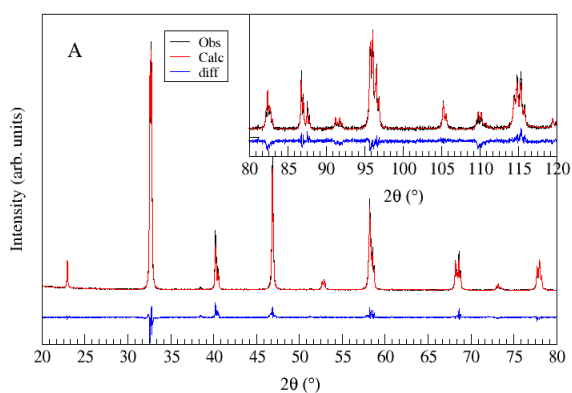


Fig.1. LSCF0.2 sample. In the inset, an enlargement of XRD data highlighting the excellent agreement between the observed and the calculated pattern.

LSCF samples can be refined in the rhombohedral R-3C^h or in the cubic Pm3^m space group. The cubic symmetry exists at high temperature and in the presence of oxygen vacancies, but can also be stabilized under vacuum (10⁻⁵ mbar) down to RT.^{19a-h,20} Since almost all diffraction peaks of rhombohedral and cubic symmetry overlap, the determination of the crystallographic phase is not straightforward. In this respect, the presence of the (113) peak at 38.5°, diagnostic of the rhombohedral arrangement, ensures the structural refinement in the R-3C^h space group. Further details are reported in the supporting information file (Fig. 1s).

The Rietveld refinement of LSCF0.2 is shown in Fig. 1 and the XRD patterns of all the samples are reported in Fig.2 (left panel) along with the respective refinements and specific enlargements in the right panel; the obtained structural parameters are reported in Table 1. By inspection of Table 1, it is evident that the LSCF0.2 and LSCF0.2-Pd samples have very similar lattice parameters, no matter of the Pd content; the same holds for LSCF0.8 and LSCF0.8-Pd. Then, the possible insertion of Pd⁴⁺ cation (as will be argued below from the EXAFS and XPS evidences) does not produce any appreciable shift of the diffraction peaks. This is not surprising because, not to mention the small Pd total concentration and the heavy-metal LSCF composition, the ionic radius of Pd⁴⁺ matches that of the iron cation.²¹ It is worth of note that the SrCO₃ phase is absent in the diffraction patterns of all samples, contrary to what reported in a previous work.²²

Table 1. Unit cell parameters, occupancy and crystallite size *d* obtained by Rietveld refinement of XRD data. The agreement factors *R*% are also reported. The error is given in parenthesis.

	<i>a</i> (Å)	<i>b</i> (Å)	<i>c</i> (Å)	<i>d</i> (Å)	Oc (Fe/Co)	<i>R</i> %
LSCF0.2	5.444 (1)	5.444 (1)	13.243 (3)	1882	0.2/0.8	4.07
LSCF0.2Pd	5.445 (1)	5.445 (1)	13.238 (5)	1018	0.2/0.8	5.05
LSCF0.8	5.499 (1)	5.499 (1)	13.358 (2)	1945	0.77/0.23	4.75
LSCF0.8Pd	5.499 (1)	5.499 (1)	13.361 (3)	1887	0.77/0.23	5.97

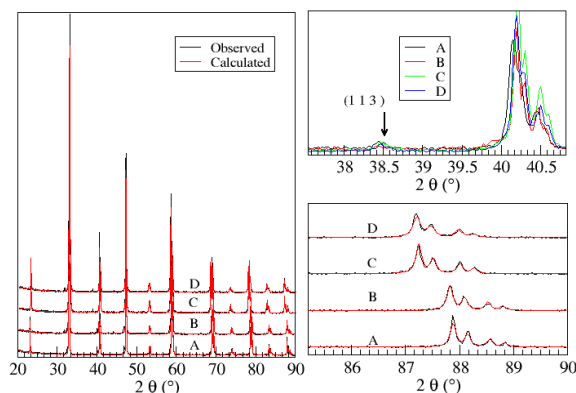


Fig.2. Left panel: XRD pattern reported up to 90° of A B C and D

(LSCF0.2, LSCF0.2-Pd, LSCF0.8 and LSCF0.8-Pd, respectively) samples. Bottom right panel: high-angle features of the rhombohedral phase. Top right panel: (113) reflection, diagnostic of rhombohedral phase, marked by arrow.

Hardly observable peaks, at angular positions in agreement with literature data for similar samples prepared by the citrate technique,²² have been attributed to very small amounts of SrLaCoO₄ and SrLaFeO₄ phases. The possible segregation of even smaller amounts of lanthanum oxide or strontium carbonate couldn't be detected. It is worth noticing that metallic palladium has its main (111) and (200) peaks at about 40.1° and 46.7° 2θ, respectively, so overlapping with LSCF reflections: taking into account that this phase is present in low concentration and in likely nanometric dispersion, it is feasible that clear evidences of its presence could not be observed in the XRD patterns.

EXAFS

Fig. 3 shows that the difference between the experimental LSCF0.8-Pd Fourier transform and the simulated Pd metal radial distribution function cannot be ascribed to the PdO signal, while in the Supporting Information it is shown that the Pd K-edge XANES and EXAFS spectra could not be analysed on the basis of a model allowing for Pd metal and PdO contributions (Fig. 2s-3s). The possibility that oxidized Pd is present in a PdO phase was then definitely discarded. Actually, the analysis of EXAFS and XANES data reported below allowed to conclude that, in agreement with similar evidences on LaFe_{0.57}Co_{0.38}Pd_{0.05}O₃,¹¹ the local environment of Pd is shared between contributions from Pd metal and oxidized Pd in the perovskite B site.

The perovskite-like structure is made up of a three-dimensional array of tilted corner-sharing Co/FeO₆ octahedra. Lanthanum (A site) is situated in the cavities formed by the octahedral units. Fig. 4 reports the perovskite fragment, bearing the Pd atom in B position, which is used to calculate amplitudes and phase shifts needed for the fitting of EXAFS data. Full details about the environment of Pd in LSCF are given in Table 2. According to the model showed in Figure 4, two γ^2 terms were allowed, taking into account the six-fold Pd-O distance (R6) at ~1.9 Å and the eight-fold R7 Pd-La coordination at 3.34 Å; moreover, one six-fold three-body configuration arising from the Pd-O-M alignment ($\theta_4=170^\circ$), with a Pd-M (M=Co or Fe) long bond at ~3.8 Å, was considered for the most important multiple scattering

contribution. It is worth noticing that these configurations are suitable to fit also the data collected at the Fe and Co K-edge.

Fig. 3. Fourier Transform uncorrected for phase shift of the sample LSCF0.8-Pd. The Pd metal component (red) and the difference pattern (blue) are shown. The Pd oxide pattern (green) is reported for comparison. (see supporting information).

Due to the large average size of the LSCF particles, as deduced from the XRD data, the fraction of surface undercoordinated atoms is negligible and therefore the coordination numbers of the perovskite phase were fixed during the fitting procedure to the respective crystal structure values. On the contrary, for the metal particles the number of neighbours was parameterized as a function of size d^{23-24} and, considering that the Pd phase did not give any clearly recognizable XRD signal, their diameter in the EXAFS model was limited in the range below 4.0 nm. Under the assumption that the only Pd environments are Pd-in-perovskite and Pd-in-metal-clusters, the relative amounts of the two phases was determined in the EXAFS fittings by a weight parameter W ranging in the 0-1 interval. The optimized model parameters are reported in Table 2, while Fig.5 details the component fitting signals for LSCF0.8-Pd.

The results relative to the Pd-Pd coordination numbers (N1-N4 in Table 2), corroborated by the good agreement of the fitting (see Figure 6), according to the χ^2 values, demonstrate that the mean dimension of Pd metal clusters is about 2 nm for both the LSCF-Pd samples. According to the weight parameter W , a Pd atomic fraction of 45% in LSCF0.2-Pd and of 62% in LSCF0.8-Pd is arranged in the B-perovskite site, suggesting that the amount of dissolved Pd is a function of iron content. This observation is not surprising, as long as iron plays an important role in stabilization of the perovskite structure and inhibition of palladium particles growth.²⁵ A very short B-site Pd-O distance of about 1.9 Å results from the EXAFS analysis. This distance is definitely different from the shortest Pd-O distance in palladium oxide (2.02 Å), pointing to a high Pd oxidation state and, moreover, the pattern of next-neighbor distances, determined by EXAFS analysis of the reference sample (Table 2), does not fit to the experimental data. Figure 6 reports the good agreement between data and structural model for both the LSCF-Pd samples.

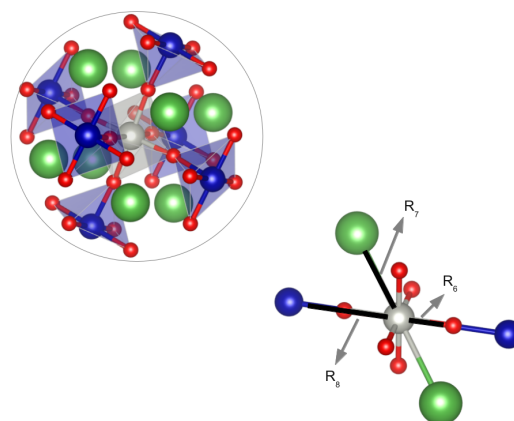
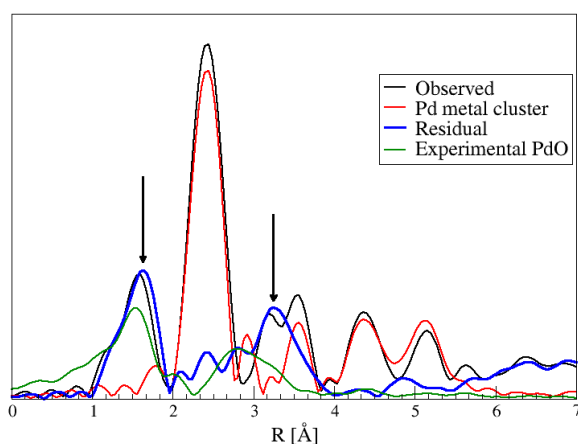


Fig. 4. Right Part: framework of perovskite structure used to calculate EXAFS amplitudes and phase shifts. Pd is gray, O is red and M (Co/Fe) is blue. The Pd atom is in the center of the sphere. In black are reported the main distances which characterize the local environment of Pd in the perovskite structure. The R_6 distance involves an important multiple scattering contribution due to co-linearity of the Pd (gray), O (red) and M (Co/Fe blue) atoms. Left Part: sketch of Pd local environment in the perovskite phase.

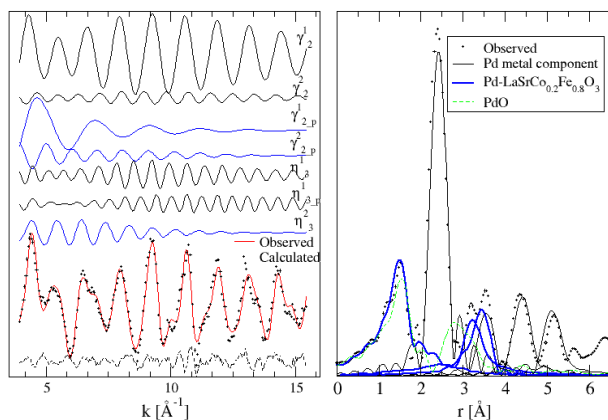


Fig. 5. Details of the calculated components used in the fitting procedure of the sample LSCF-0.8Pd. Left Panel shows the EXAFS signals of Pd metal clusters (black solid line), and perovskite phase (Pd-O, Pd-La and Pd-O-Pd distances are reported in blue solid lines). The γ and the η are the two body and three configuration functions respectively. Right Panel: Fourier Transform of the signals showed in the left panel (black metal Pd, blue Pd-O, Pd-La and Pd-O-Pd distances in the perovskite). For comparison reason also the PdO (dash green) spectrum has been inserted.

Taking into account that the ionic radii of Pd^{2+} , Pd^{3+} and Pd^{4+} in six-fold coordination are respectively 0.86 Å, 0.76 Å and 0.62 Å while the ionic radius of O^{2-} is ~1.40 Å,²¹ it can be concluded that oxidized palladium in the LSCF B-site is likely in the 4+ oxidation state, in agreement with our XPS results (vide infra) and with previously reported data on similar compounds.²⁵ This is also consistent with the observed chemical shift of the absorption edge (Fig. 2s).

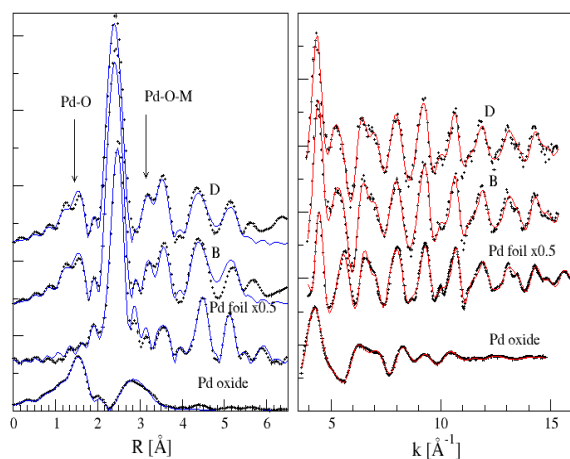


Fig.6. The fitting of the data of the sample LSCF0.2-Pd (B) and LSCF0.8-Pd (D) as described in the text is showed.

The values of Pd-Pd distance ($r=2.74$ Å) reported here are coherent with the existence of Pd metal clusters. EXAFS analysis relative to reduced $\text{LaFe}_{0.57}\text{Co}_{0.38}\text{Pd}_{0.05}\text{O}_3$ catalysts pointed out the possible formation of Pd-Co solid solution as a consequence of Co segregation and formation of secondary crystallographic phase such as La_2O_3 and $\text{La}(\text{OH})_3$.¹¹ Similar alloying effects between supported metal and reducible oxides after suitable reduction treatment were demonstrated also for other systems,²⁶ but in this case a specific reductive treatment for an EXAFS experiment was not carried out. Also the small Pd concentration may justify the absence of clear evidences of a Pd-Co solid solution formation.

It is worth noticing the stability of incorporation of Pd as tetravalent cation in the perovskite B site, able to overcome lengthy and high-temperature treatments. This finding points to the advantages of the citrate one pot preparation method of synthesis that allows the stabilization of a portion of Pd cation within the LSCF lattice at a temperature (of about 800 °C) that is higher than the temperature of thermal decomposition of PdO to Pd metal.

Table 2 Results from the EXAFS fits where the errors are in the last digit. N indicates the calculated coordination numbers according to the Borowsky's equation²³, d is the dimension of metallic Pd and W indicates the fraction of Pd in-perovskite phases.

	Pd in metal clusters		Reference sample
	LSCF0.2Pd	LSCF0.8Pd	Pd Foil
$R_{1-Pd-Pd}(\text{Å})$	2.742	2.740	2.744
$\sigma_1^2(\text{Å}^2)$	0.0010	0.0010	0.0013
$R_{2-Pd-Pd}(\text{Å})$	3.878	3.877	3.881
$\sigma_2^2(\text{Å}^2)$	0.0024	0.0024	0.0029
$\Theta_{1-Pd-Pd-Pd}(\text{°})$	120.9	120.9	120.4
	$R_3=4.772$	$R_3=4.771$	$R_3=4.764$
	$\sigma_3=0.00278$	$\sigma_3=0.0034$	$\sigma_3=0.0025$
$\Theta_{2-Pd-Pd-Pd}(\text{°})$	177.8	177.7	177.8
	$R_4=5.480$	$R_4=5.480$	$R_4=5.474$
	$\sigma_4=0.0020$	$\sigma_4=0.0020$	$\sigma_4=0.0026$
$\Theta_{3-Pd-Pd-Pd}(\text{°})$			60.0
			$R_5=2.757$
			$\sigma_5=0.0082$
N_1	8.2	8.2	12
N_2	3.8	3.9	6
N_3	16.8	17.0	24
N_4	7.9	7.9	12
$d(\text{Å})$	20	21	
	Pd in LSCF		
$R_{6-Pd-O}(\text{Å})$	1.911	1.930	
$\sigma_6^2(\text{Å}^2)$	0.0043	0.0040	
$R_{7-Pd-La-Pd-Sr}(\text{Å})$	3.345	3.346	
$\sigma_7^2(\text{Å}^2)$	0.0093	0.0094	
$\Theta_{4-Pd-O-M}(\text{°})$	170.0	170.0	
$M=\text{Fe, Co, Pd}$	$R_{8-Pd-M}=3.808$	$R_{8-Pd-M}=3.846$	
	$\sigma_8=0.0086$	$\sigma_8=0.0079$	
W	0,45	0,62	
$R_{Pd-O}(\text{Å})$			PdO
$\sigma^2(\text{Å}^2)$			1.994
			0.0010

$R_{\text{Pd-Pd}} (\text{\AA})$	3.047
$\sigma^2 (\text{\AA}^2)$	0.0093
$R_{\text{Pd-Pd}} (\text{\AA})$	3.373
$\sigma^2 (\text{\AA}^2)$	0.0073

XPS

X-ray photoelectron spectroscopy was performed in order to study the chemical state and surface composition of the synthesized materials. Table 3 reports the binding energies of elements constituting the catalysts. The O 1s peak (Figure 7), typical of all perovskitic materials, consists of three components at about 529, 531 and 532 eV which are usually attributed to lattice, surface, and adsorbed oxygen respectively.²⁷⁻²⁹ The relative concentrations of lattice and surface oxygen are reported in Table 1, showing the decrease of the former component in Pd doped samples.²⁹ The variation is definitely more pronounced in the LSCF0.2 series. Interestingly, both Sr 3d and La 3d peaks show complex features (see discussion in the supporting information file) despite the unique possible oxidation state of the two anions.³⁰ In LSCF, the B position is occupied by iron or cobalt, in the two oxidation states 2^+ and 3^+ whose relative amount could be estimated only for the ion present in higher concentration, that is Fe for LSCF0.8 and Co for LSCF0.2. For LSCF0.8 the Fe 2p peak fitting was performed according to the constraints for the Fe^{2+} and Fe^{3+} components and the respective shake up satellites indicated by Lin³⁰; the results are summarized in Table 3 and showed in Fig. 7s of the supporting information. Both samples show the two oxidation states characterized by the components at 710.0 eV and 711.8 eV for Fe^{2+} and Fe^{3+} respectively. The relative concentration of Fe^{2+} increased with the insertion of Pd (see Table 1). For the low iron concentration sample, the peak intensity is so low that it is not possible to achieve a reliable determination of the two oxidation states. Analogously, the Co 2p region was fitted with the Co^{2+} , Co^{3+} and the respective shake up satellites.^{31,32} In the case of cobalt, the Co^{2+} component is located at higher binding energy than the Co^{3+} (783 vs. 780 eV)³¹ (see Fig. 7s a) of supporting information).

The addition of a small quantity of Pd causes an increase of the Co and Fe bivalent oxidation state, as displayed in Table 3; moreover, the Pd3d region (see Fig. 6s of supporting information) shows that the Pd doublet is centered at 338 eV for both LSCF-Pd samples. This value is higher than the corresponding binding energy of Pd^{2+} and, in agreement with the EXAFS results, can be ascribed to Pd^{4+} inserted in the perovskite network.³³ No Pd^0 or Pd^{2+} were detected by XPS in the LSCF electrocatalysts while EXAFS was able to see very small Pd metal clusters but, like XPS, did not evidenced the presence of a PdO phase. The absence of Pd metal particles from the surface is likely due to oxidation during the cooling down in air following the calcination treatment.³⁴ Then, considering the combined EXAFS and XPS evidences, it seems feasible to conclude that oxidized Pd can exist only as Pd^{4+} in the perovskite B-site, whereas Pd^0 is present as

nanostructured clusters embedded in the perovskite matrix. XPS analysis carried out on the LSCF-Pd perovskites calcined at 800 °C evidenced as well a Pd doublet centered at 338 eV, suggesting that the Pd^{4+} can be already inserted into the perovskite lattice at the temperature at which crystallization of the perovskite takes place. Table 4 shows the relative atomic percentages of the different elements. As already reported for similar materials, strontium segregates on the surface with a general Sr enrichment with respect to the stoichiometric amount.^{22,35,36} In B position the Co concentration is similar to the stoichiometric amount, while iron diffuses into the bulk and its surface concentration is lower than the nominal.

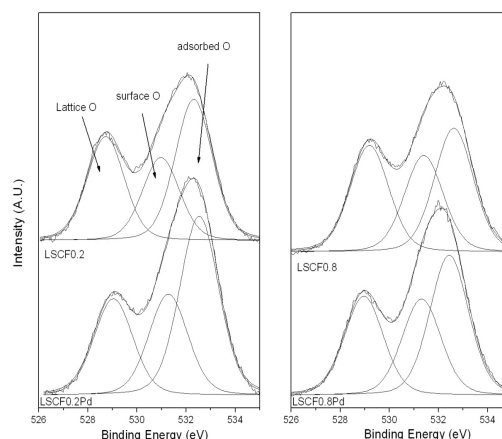


Fig. 7. O1s high resolution region. The peak due to physisorbed oxygen was omitted in the oxygen quantification.

Table 3. Binding energy of La 3d5/2, Sr 3d5/2, Co 2p3/2, Fe 2p3/2, O1s and Pd 3d5/2 of samples. In parenthesis the relative percentage of peaks, when more components are present, is given. For La 3d5/2 the satellite over main peak area ratio is given.

	La 3d 5/2	Sr 3d5/2	Co 2p3/2	Fe 2p3/2	O 1s	Pd 3d5/2
LSCF0.2	833.3 SII/M= 0.29	132.3 (59) 133.7 (41)	782.9 (58) 780.1 (42)	710.0	528.6 (55) 530.9 (45)	
LSCF0.2Pd	833.7 SII/M= 0.16	132.6 (65) 134.6 (35)	783.0 (62) 780.3 (38)	710.4	529.0 (48) 531.3 (52)	338.0
LSCF0.8	834.0 SII/M= 0.16	132.8 (63) 134.7 (37)	781.2	710.0 (54) 711.8 (46)	529.1 (52) 531.5 (48)	-
LSCF0.8Pd	SII/M= 0.34	134.2 (38)	781.0	710.0(67) 711.8(33)	528.9(50) 531.5(50)	338.4

Table 4. Surface atomic compositions of samples as measured by XPS; nominal concentrations are given in parenthesis.

	La	Sr	Co	Fe	Pd	O
LSCF0.2	0.09 (0.12)	0.19 (0.08)	0.11 (0.16)	0.01 (0.04)	-	0.60 (0.6)
LSCF0.2Pd	0.07 (0.12)	0.16 (0.08)	0.11 (0.16)	0.007 (0.034)	0.007 (0.006)	0.64 (0.6)
LSCF0.8	0.07 (0.12)	0.16 (0.08)	0.03 (0.04)	0.05 (0.16)	-	0.68 (0.6)
LSCF0.8Pd	0.05 (0.12)	0.17 (0.08)	0.03 (0.04)	0.04 (0.154)	0.010 (0.006)	0.67 (0.6)

TPR

H₂-TPR curves for LSCF and LSCF-Pd perovskites are displayed in Figure 8. The hydrogen consumption and reduction temperature peaks are presented in Table 1s (see supporting information file). Since La³⁺ and Sr²⁺ are not reducible under the conditions of H₂-TPR, the observed H₂ consumption peaks in the TPR profiles displayed in Fig. 8 are due to the reduction of cobalt, iron and palladium cations. Generally, the peaks comprised in the interval 300-600 °C are related to the reduction of Co³⁺ → Co²⁺, those in the range 600-800 °C are due to the reduction Co²⁺ → Co⁰, while at around 900 °C reduction Fe³⁺ → Fe⁰ occurs in one step^{37,38}. Pd addition to LSCF0.2 produces two new peaks, at 141 and at 229 °C respectively, attributed in the LSCF0.2-Pd reduction profile to the reduction of Pd⁴⁺ species that, once reduced to metallic Pd, cooperates with the already present Pd⁰ to lowering the reduction temperature of Co³⁺ to Co²⁺. The reduction of Co²⁺ to Co⁰ and Fe³⁺ to Fe⁰ was affected to a minor extent by the presence of Pd: as reported in Table 1s, the Pd addition slightly increased the amount of Co³⁺/Co⁰ reduction from 82.5% to 86.4%, while the extent of Fe³⁺ to Fe⁰ reduction remained almost constant near 85%. In the reduction profile of LSCF0.8-Pd a peak at 121 °C attributed to the concomitant reduction of Pd⁴⁺ species and Co³⁺ to Co⁰ was observed. A small peak at 445 °C due to the reduction of residual Co³⁺ species was still detected. As previously observed for LSCF0.2-Pd, a minor effect on the Fe³⁺ reduction, in terms of reduction temperature, was played by the presence of Pd. However, inspection of Table 1s evidences that the presence of Pd in the LSCF0.8 perovskite enhanced significantly the full reduction of Co³⁺ and Fe³⁺ from 59.6 to 73% and from 50 to 56.5%, respectively.

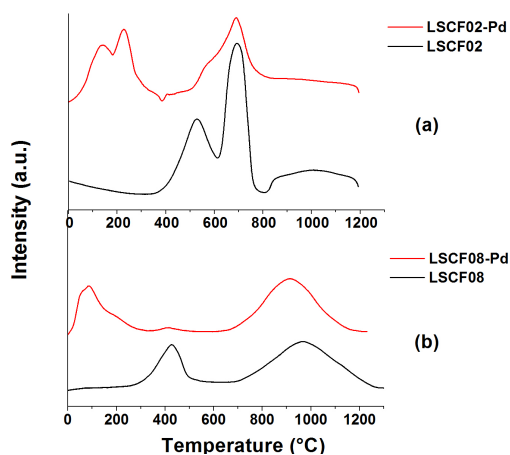


Fig.8. TPR profiles for unpromoted and Pd promoted LSCF0.2 (a) and LSCF0.8 perovskites (b) respectively.

Oxygen storage capacity (OSC) and Thermogravimetric analysis (TGA)

Oxygen pulses chemisorption experiments, carried out at 600 °C over the LSCF and LSCF-Pd samples aimed to investigate the oxygen storage capacity at a temperature that could be of interest for oxygen reduction on cathode-type materials. The results listed in Table 5 highlight the high oxygen vacancies content of all the above mentioned oxides, especially for LSCF08 and LSCF08-Pd. Moreover, it is worth noting that the oxygen chemisorption capability of LSCF-Pd samples is higher than the corresponding LSCF samples, especially by comparing LSCF02 and LSCF02-Pd. In the

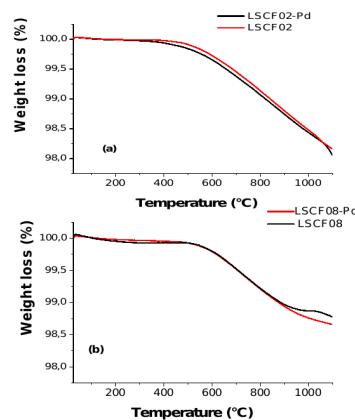


Fig.9. Weight loss (%) versus temperature registered during TGA experiments carried out under N₂ flow for LSCF and LSCF-Pd samples: (a) LSCF02 and LSCF02-Pd; (b) LSCF08 and LSCF08-Pd.

reduction profile of LSCF0.8-Pd a peak at 121 °C attributed to the concomitant reduction of Pd⁴⁺ species and Co³⁺ to Co⁰ was observed. A small peak at 445 °C due to the reduction of residual Co³⁺ species was still detected. As previously observed for LSCF0.2-Pd, a minor effect on the Fe³⁺ reduction, in terms of reduction temperature, was played by the presence of Pd. However, inspection of Table 1s evidences that the presence of Pd in the LSCF0.8 perovskite enhanced significantly the full reduction of Co³⁺ and Fe³⁺ from 59.6 to 73% and from 50 to 56.5%, respectively.

The increase of oxygen vacancies content in presence of Pd was also suggested by carrying out TGA experiments. It was confirmed that LSCF08 and LSCF08-Pd showed the highest oxygen chemisorption capacity giving the highest weight loss (see Table 5). Once again a beneficial effect was played by Pd.

Table 5. Results of OSC and TGA analysis.

Sample	O ₂ chemisorbed values (ml/g) at 600 °C	Weight loss (%) due to O ₂ release
LSCF02	82.5	82.5
LSCF02-Pd	86.4	86.4
LSCF08	59.6	59.6
LSCF08-Pd	73.0	73.0

LSCF02	2,2	1,90
LSCF02-Pd	2,5	2,05
LSCF08	1,1	1,21
LSCF08-Pd	1,3	1,35

DISCUSSION

The present study reports the first example of LSCF-Pd materials prepared by adding a Pd precursor in one pot synthesis, with a final product characterized by the co-existence of cationic Pd⁴⁺ species stabilized into the perovskite lattice and dispersed Pd metal nanoclusters of about 2 nm in size embedded in the oxide matrix. The coexistence of zero and positive palladium valence states was already observed in the case of the Pd cobalt-ferrite, ruled by a dynamical equilibrium between the two oxidation states depending on the reductive or oxidative environment,¹¹ and in other metal catalysts supported on reducible oxides.^{26,39}

The insertion of Pd as tetravalent cation in the perovskite lattice, leading to a net electronic transfer to the matrix, could be a consequence of a strong electronic interaction established between sub-nanometric Pd metal clusters and the reducible oxide.⁴⁰ These cations can migrate inside the perovskite lattice by a mechanism of polaronic distortion. Hence, it can be argued that a dynamical equilibrium Pd⁰-Pd⁴⁺ could be effective, depending on O₂ partial pressure.

As observed by XPS, LSCF-Pd show increased [Co²⁺]/[Co³⁺] and [Fe²⁺]/[Fe³⁺] ratios with respect to Pd-free samples, thus producing a reorganization of the electronic structure of the catalysts involving an enhancement of oxygen vacancies and a decrease of electron holes concentration. In fact, XPS measurements evidenced the effective increase of surface oxygen vacancies in the LSCF-Pd samples, a result confirmed also by OSC and TGA. Then, insertion of Pd⁴⁺ in the B-perovskite site have a positive effect on the dissociative oxygen adsorption in the perovskite surface vacancies. This mechanism could be effective at high O₂ partial pressure, involving charge transfer from the oxide to adsorbed oxygen, with the consequent formation of electronic holes (h[•]), related to re-oxidized Fe and Co cations. In this respect, the presence of bulk oxygen vacancies can favour the diffusion of O²⁻ from the surface, so making available fresh adsorption sites for O₂. On the other hand, it is possible that a strong O²⁻-Pd⁴⁺ attraction, hindering oxygen diffusive paths, takes place, so that the best performance as cathodic material is reached by insertion of an optimal amount of Pd⁴⁺. Then, beside possible different morphologies between LSCF0.2-Pd and LSCF0.8-Pd, the lower OSC of the latter could be ascribed to an excess concentration of Pd⁴⁺ sites. In closed circuit conditions the electrons for the cathodic reaction are provided by the external circuit, so producing a steady O₂ reduction cycle. It should also be pointed out that the Pd nanometric metal phase does not undergo phenomena of particle coalescence after drastic thermal treatments, confirming the strong interaction with the support and, in view of possible applications, ensuring the long-term stability of Pd-LSCF materials for the exploitation as FC cathode materials.

Further investigations on the structural, electronic and electrochemical properties of a series of LSCF Pd-doped oxides with different composition of Co and Fe are in progress.

Conclusions

The present study reports the first example of LSCF-Pd perovskites prepared by adding Pd precursor in one pot synthesis and characterized by the presence of cationic Pd⁴⁺ stabilized into the perovskite lattice and Pd nanometric particles (around 2 nm) well dispersed and strongly interacting with the oxide.

The nanostructured La_{1-x}Sr_xCo_{1-y}Fe_{y-0.03}Pd_{0.03}O_{3-δ} (LSCF-Pd) perovskites were accomplished with fixed La-Sr composition (x=0.4) and two different Fe contents (y= 0.2 and 0.8). The promotion of La_{0.6}Sr_{0.4}Co_{0.8}Fe_{0.2}O_{3-δ} and La_{0.6}Sr_{0.4}Co_{0.2}Fe_{0.8}O_{3-δ} by incorporation of palladium in the B-site of the perovskite structure was evidenced by solving the local environment of Pd. The nanometric Pd metal phase is likely in dynamical equilibrium, depending on the O₂ partial pressure, with the Pd⁴⁺ cations inserted in the perovskite structure, and does not undergo coalescence after high temperature prolonged thermal treatments. OSC measurements demonstrate the beneficial role of Pd insertion for the formation of bulk oxygen vacancies that increased oxygen chemisorption capability of such materials.

Notes and references

^a Dipartimento Fisica e Chimica Università di Palermo Viale delle Scienze Ed. 17, 90128 PALERMO, Italy.

^b ISMN-CNR, UOS Palermo, Via Ugo La Malfa, 153, 90146 Palermo, Italy

^c Dutch-Belgian Beamline (DUBBLE), European Synchrotron Radiation Facility (ESRF), B.P. 220, F-38043 Grenoble, France.

^d Netherlands Organization for Scientific Research (NWO), ESRF-The European Synchrotron CS40220 38043 Grenoble Cedex 9 France.

† Electronic Supplementary Information (ESI) available: [details of any supplementary information available should be included here]. See DOI:10.1039/b000000x/

‡ Footnotes should appear here. These might include comments relevant to but not central to the matter under discussion, limited experimental and spectral data, and crystallographic data. 5063.

1. J.M Serra., H.-P. Buchkremer, *J. Power Sources*, 2007, **72**,768..
2. S. B. Adler, *Chem. Rev.*, 2004, **104**, 4791.
3. S. B. Adler, X.J. Chen, J.R. Wilson, *J. Catal.* 2007, **245**, 91.
4. E. Ivers-Tiffée, A. Weber, H. Schichlein, in: W. Vielstich, A. Lamm, H.A. Gasteiger (Eds.), *Handbook of Fuel Cells*, 2003, **2**, 587.
5. P. J. Gellings, H. J. M Bouwmeester, *Catal. Today*, 2000, **58**, 1.
6. F. S. Baumann, J. Fleig, H. U. Habermeier, J. Maier, *Solid State Ionics* 2006, **177**, 1071.
7. J. Chen, F. Lianga, B. Chi, J. Pu, S. P. Jiangb, L. Jian, *J. Power Sources*, 2009, **194**, 275.
8. Y. Sakito, A. Hirano, N. Imanishi, Y. Takeda, O. Yamamoto, Y. Liu, *J. Power Sources*, 2008, **182**, 476.
9. M. Sahibzada, S. J. Benson, R. A. Rudkin, J. A. Kilner, J.A.; *Solid State Ionics*, 1998, 115,.
10. R. Zhang, A. Villanueva, A. Alamdari, S. Kaliaguine, *J. Catal.*, 2006, **237**, 368.
11. Y. Nishihata, J. Mizuki, T. Akao, H. Tanaka, M. Uenishi, M.

- Kimura, T. Okamoto, N. Hamadok, *Nature*, 2002, **418**, 164.
12. Q. Xu, D. Huang, W. Chen, J. Lee, JH. Wang, R. Yuan, *Scripta Materialia*, 2004, **50**, 165.
13. A. Larson, R. B. Von Dreele, *Los Alamos National Laboratory Report LAUR*, 2000, 86.
14. S. Nikitenko, A. M. Beale, A. M. J. van der Eerden, S. D. M. Jacques, O. Leynaud, M. J. O'Brien, D. Detollenaere, R. Kaptein, B. M. Weckhuysen, W. Bras, *J. Synchrotron Rad.*, 2008, **15**, 632–640.
15. A. Filipponi, A. Di Cicco, C. R. Natoli, *Phys. Rev. B*, 1995, **52**, 15122.
16. Filipponi, A.; Di Cicco, A.; *Phys. Rev. B* **1995**, *52*, 15135-15149.
17. D. A. Shirley, *Phys. Rev. B*, 1972, **5**, 4709.
18. P. M. A. Sherwood, *Practical Surface Analysis*, 1990, 181.
19. a) M. M. Natile, F. Poletto, A. Galenda, A. Glisenti, T. Montini, L. De Rogatis, P. Fornasiero, *Chem. Mater.*, 2008, **20**, 2314; b) J. C. Grenier, N. Ea, M. Pouchard and P. Hagemuller, *J. of Solid State Chem.* 1985, **58**, 243; c) J. M. Gonzalezcalbet, M. Parras, M. Valletregi and J. C. Grenier, *J. of Solid State Chem.* 1990, **86**, 149; d) N. Orlovskaya, N. Browning and A. Nicholls, *Acta Materialia* 2003, **51**, 5063; e) A. Fossdal, M. Menon, I. Waernhus, K. Wiik, M. A. Einarsrud and T. Grande, *J. American Ceram. Soc.* 2004, **87**, 1952. f) W. Shaorong, M. Katsuki, M. Dokiya, T. Hashimoto, *Solid State Ionics*, 2003, **159**, 71. g) S. Hashimoto, Y. Fukuda, M. Kuhn, K. Sato, K. Yashiro, J. Mizusaki, *Solid State Ionics*, 2010, **181**, 1713. h) A. Mineshige, J. Izutsu, M. Nakamura, K. Nigaki, J. Abe, M. Kobune, S. Fuji, T. Yazawa, *Solid State Ionics*, 2005, **176**, 1145.
20. G. H. Jonker, *Philips Res. Rep.*, 1969, **24**, 1.
21. R. D. Shannon, *Acta Crystallogr. A*, 1976, **32**, 751.
22. R. Bertacco, J. P. Contour, A. Berthelemy, J. Olivier, *Surf. Sci.*, 2002, **511**, 366.
23. M. Borowski, *J. Phys.*, 1997, **IV(7)**, **C2**, 259.
24. A. Longo, L. F. Liotta, G. Pantaleo, A. Venezia, F. Giannici, A. Martorana, *J. Phys. Chem. C*, 2012, **116**, 2960.
25. Y. Nishihata, J. Mizuki, H. Tanaka, M. Uenisci, M. Kimura, *J. Phys. Chem. Solids*, 2005, **66**, 274.
26. G. Deganello, F. Giannici, A. Martorana, G. Pantaleo, A. Prestianni, A. Balerna, L. F. Liotta, A. Longo, *J. Phys. Chem. B*, 2006, **110**, 8731.
27. X. Li, H. Zhang, X. Liu, S. Li, M. Zhao, *Mater Chem. Phys.*, 1994, **38**, 355.
28. X. Li, X. Liu, B. Zu, M. Zhao, *J. of Alloys and Compounds*, 1992, **186**, 315.
29. D. H. Prasad, S. Y. Park, E. O. Oh, H. R. Kim, K. J. Son, J. H. Lee, *Appl. Catal. A*, 2012, **447-448**, 100.
30. B. Liu, L. Tanga, Y. Zhanga, *Int. J. of Hydrogen Energy*, 2009, **34**, 440.
31. T. C. Lin, G. Seshadri, J. A. Kelber, *Appl. Surf. Sci.*, 1997, **119**, 83.
32. Y. Lin, L. Liu, H. Zhang, X. Yao, F. Gao, K. Yao, L. Dong, *J. Colloid Interface Sci.*, 2013, **390**, 158.
33. M. Uenishi, M. Taniguchi, H. Tanaka, M. Kimura, Y. Nishihata, J. Mizuki, T. Kobayashi, *Appl. Catal. B*, 2005, **57**, 267.
34. S. Eriksson, M. Boutonnet, S. Järås, *Appl. Catal. A*, 2006, **312**, 95.
35. J. M. Giraudon, A. Elhachimi, F. Wyrwalski, S. Siffert, A. Abouka, J. F. Lamonier, G. Leclercq, *Appl. Catal. B*, 2007, **75**, 157.
36. P. A. W. Ven der Heide, *Surf. Interface Anal.*, 2002, **33**, 414.
37. S. Royer, F. Bérubé, S. Kaliaguine, *Appl. Catal. A: General*, 2005, **282**, 273.
38. B. Levasseur, S. Kaliaguine, *Appl. Catal. A: General*, 2008, 343, 29.
39. Levasseur, B.; Kaliaguine, S.; *Appl. Catal. A: General*, 2008, 343, 29.
40. S. Bernal, J. J. Calvino, M. A. Cauqui, J. M. Gatica, C. Larese, J. A. Pérez Omil, J. M. Pintado, *Catal. Today*, 1999, **50**, 175.
41. G. Pacchioni, *Phys. Chem. Chem. Phys.*, 2013, **15**, 1737.